ACS APPLIED MATERIALS & INTERFACES

Research Article

www.acsami.org

Electrically Conductive Polypropylene Nanocomposites with Negative Permittivity at Low Carbon Nanotube Loading Levels

Xi Zhang,[†,‡,§] Xingru Yan,[†] Qingliang He,[†,▽] Huige Wei,[†,‡,§] Jun Long,[§] Jiang Guo,[†] Hongbo Gu,[∥] Jingfang Yu,[⊥] Jingjing Liu,[⊥] Daowei Ding,[†,▽] Luyi Sun,[⊥] Suying Wei,*[,‡,§] and Zhanhu Guo*[,†]

[†]Integrated Composites Laboratory (ICL), Department of Chemical and Biomolecular Engineering, University of Tennessee, Knoxville, Tennessee 37996, United States

[‡]Department of Chemistry and Biochemistry and [§]Dan F. Smith Department of Chemical Engineering, Lamar University, Beaumont, Texas 77710, United States

[∥]Department of Chemistry, Tongji University, Shanghai, 200092, China

[⊥]Institute of Materials Science, University of Connecticut, Storrs, Connecticut 06269, United States

[▽]Engineered Multifunctional Composites, LLC, Beaumont, Texas 77713, United States

Supporting Information

ABSTRACT: Polypropylene (PP)/carbon nanotubes (CNTs) nanocomposites were prepared by coating CNTs on the surface of gelated/swollen soft PP pellets. The electrical conductivity (σ) studies revealed a percolation threshold of only 0.3 wt %, and the electrical conductivity mechanism followed a 3-d variable range hopping (VRH) behavior. At lower processing temperature, the CNTs formed the network structure more easily, resulting in a higher σ. The fraction of γ-phase PP increased with increasing the pressing temperature. The CNTs at lower loading (0.1 wt %) served as nucleating sites and promoted the crystallization of PP. The CNTs favored the disentanglement of polymer chains and thus caused an even lower melt viscosity of nanocomposites than that of pure PP. The calculated optical band gap of CNTs was observed to increase with increasing the processing temperature, i.e., 1.55 eV for nanocomposites prepared at 120 °C and 1.70 eV prepared at 160 and 180 °C. Both the Drude model and interband transition phenomenon have been used for theoretical analysis of the real permittivity of the nanocomposites.

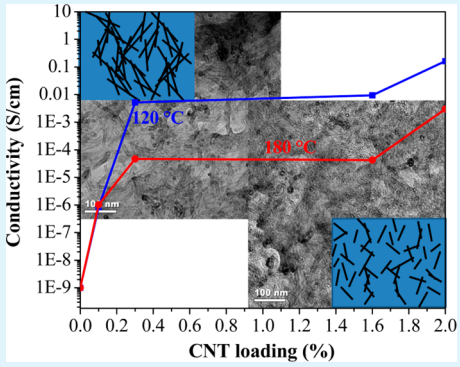

KEYWORDS: *polypropylene nanocomposites, percolation value, crystal phases, viscosity, band gap, negative permittivity*

1. INTRODUCTION

The development of conductive or semiconductive polymer nanocomposites (PNCs) has attracted more interest due to the introduced unique physicochemical properties to the otherwise inert hosting polymers such as thermal stability[1−3] and magnetic,[4,5] optical,[6,7] electrochromic,[8−10] and dielectric properties.[11,12] Generally, the conductive PNCs have been prepared by introducing conductive nanofillers to the insulating polymer matrix. Among all the conductive nanofillers, carbon nanotubes (CNTs) show excellent physical properties such as high aspect ratio (1000)[13] and great tensile strength and Young's modulus (1 TPa).[13] Compared with metal nanofillers, CNTs with higher flexibility and lower density can enhance the mechanical, thermal, and conductive properties of the polymers including polypropylene (PP).[13,14] For instance, by limiting the crack propagation, the CNTs enhanced the yield stress and Young's modulus of PP.[13] CNTs have also served as flame retardants. For example, the network layer of the MWCNT protected the inner PP layer by reducing the heat flux transmission.[15] However, due to the poor dispersion of CNTs, a high CNT content is required to accomplish the conduction network in the polymer matrix.[16,17] For instance, when PP was melt blended with MWCNTs, the electrical percolation threshold was achieved with a CNTs loading between 1.0 and 2.0 wt %, and the volume resistivity of the PNCs with 5.0 wt % CNTs was still above 100 ohm·cm.[18] The PP/MWNTs nanocomposites obtained by in situ polymerization did not reach percolation even at a CNT loading of 3.5 wt % with a reported resistivity of about 1×10^{15} ohm·cm.[19] Although a low percolation threshold of 0.097 vol % for the CNTs in the polyester resin was reported from the rheological investigation,[20] it would be more interesting to obtain the percolation threshold from the aspect of electrical conductivity to present the real percolating situation considering the wrapping of polymer chains around the CNTs to give a lower viscosity percolation value as observed in the epoxy nanosuspensions with carbon nanofibers (CNFs).[21] To enhance the conductivity, additional treatments have been reported including chemical functionalization with acid or amine and heating. By immersing the MWCNTs in acid or

Received: December 6, 2014
Accepted: February 26, 2015
Published: February 26, 2015

DOI: 10.1021/am5082183
ACS Appl. Mater. Interfaces 2015, 7, 6125−6138

octadecylamine solution, the MWCNTs were oxidized or grafted with amine groups, which improved the interfacial interaction between MWCNTs and polymer matrix.[22] Although annealing has removed amorphous carbon from MWCNTs,[22] the electrical percolation threshold was achieved at a treated CNTs loading between 1.0 and 2.0 wt %, and the electrical conductivity of the PNCs with 5.0 wt % was still lower than 10^{-2} S/cm.[22] However, these treatments would cause some negative effects on the conductivity of the pristine CNTs by influencing the crystalline structure and interfacial characteristics[23] or even introducing insulating layers.[21] For instance, the partially damaged crystalline structure of the MWNTs from treatment with concentrated HNO_3 and H_2O_2/NH_4OH solution to introduce the carboxylic groups caused a lower conductivity.[24]

Negative permittivity, normally observed in the negative refractive index artificially designed metal-based materials,[25] was attributed to the plasma-like resonance of free electrons on the metal surface.[26] For the CNTs exhibiting a low plasma frequency, negative real permittivity can be observed when the test frequency was lower than the plasma frequency.[27] The recently reported negative permittivity in the polyaniline− and polypyrrole−tungsten oxide[28] and CNFs/elastomer[29] PNCs, etc., was simply achieved by component incorporation rather than the traditional structure design. These materials have potential applications including cloaking, superlens, wave filters, and superconductors.[30−32] Although the optical and dielectric properties of pure CNTs have been studied due to their potential wide applications in energy storage[33] and electronic devices,[34] few reports can be found on the optical and dielectric properties of the CNTs reinforced PP PNCs, especially with a negative permittivity.

In this paper, the PP nanocomposites with a unique structure were prepared by swelling the PP powders rather than dissolving completely in the solvent to allow the surface of PP powders to exhibit a gelate state for the CNTs to stick on under an external shear force field. Then the dried PP powders wrapped with CNTs were hot pressed at 120, 160, or 180 °C to obtain the final nanocomposite finishing for tests. The melt rheological behaviors of the PNCs, including viscosity at steady state, viscosity storage, and loss moduli, and loss factor were studied. For all PNCs, the thermal stability was tested by TGA. The effects of CNTs on the crystalline structure of PP including crystal structure, crystallization temperature, and crystalline fraction were evaluated. The effects of both the CNTs loading and the processing temperature on the optical properties were studied by the Taue plot and theoretically analyzed with the strain loaded on the CNTs in the PP matrix. The unique dielectric property of the PNCs was theoretically analyzed with the popular Drude model and interband transition phenomenon for the permittivity transitions between positive and negative.

2. EXPERIMENTAL SECTION

2.1. Materials. The polypropylene (PP) used in this study was supplied by Total Petrochemicals Inc. USA (PP, grade 6824 MZ, $M_n \approx$ 40 500, $M_w \approx$ 155 000, melt index 35 g/min). The carbon nanotubes (CNTs, SWeNT SMW100; average diameter 6−10 nm; length > 1 μm; BET surface area 300−330 m^2/g) were provided by SouthWest NanoTechnologies, Inc. The solvent xylene (laboratory grade, ρ = 0.87 g/cm^3) was purchased from Fisher Scientific. All chemicals were used as received without any further treatments.

2.2. Preparation of PP/CNTs Nanocomposites. The PP/CNTs nanocomposites with 0.1, 0.3, 1.6, and 2.0 wt % CNTs were prepared. Briefly, 20 g of PP powders was dispersed in 200 mL of xylene and magnetically stirred at 70 °C for 24 h to allow the PP powders to swell completely. When the surface of the swollen PP pellet was in gelate phase and became very soft, the CNTs were added to the solution and the mixture was further stirred for 12 h. The CNTs loading in the PNCs was controlled by varying the weight of CNTs added into the above solution. Finally, extra xylene was vaporized, and the PP powders coated with CNTs were obtained. The final powders were hot pressed under a pressure of 1 psi for 30 min to form a round disk for testing. Three temperatures of 120, 160, and 180 °C were selected to study the effect of processing temperature on the physical properties of the PNCs.

2.3. Characterization. *Rheological Behaviors of the PP/CNTs Nanocomposites Melts.* The melt rheological behaviors of the nanocomposites were investigated with a rheometer (AR 2000ex, TA Instruments). An environmental test chamber (ETC) steel parallel-plate geometry (25 mm in diameter) was used to perform the measurements at shear rates ranging from 0.1 to 100 s^{-1} at 200 °C. The samples were loaded into the model when the temperature was heated to 200 °C. Dynamic rheological measurements were also performed with dynamic oscillation frequency ranging from 0.1 to 100 rad/s at a low strain (1.0%), which was justified to be within the linear viscoelastic (LVE) range for these materials. The LVE range was determined by the strain−storage modulus (G') curve within the strain range from 0.01 to 100 at a frequency of 1 rad/s.

Crystalline Structure of the PP/CNTs Nanocomposites. The crystalline structure of pure PP and its PNCs was studied by X-ray diffraction (XRD), which was carried out by a Bruker AXS D8 Discover diffractometer operating with a Cu Kα radiation source (λ = 0.154 nm). The X-ray was generated at 40 kV and 27 mA power, and the scans were recorded at 2θ from 5° to 30°. The PP/CNTs samples used for the test were molded by hot pressing the composite powders at 120, 160, and 180 °C into a cylindrical shape of 25 mm in diameter and ∼1.0 mm in thickness.

Thermal Characterization of the PP/CNTs Nanocomposites. The thermal stability of the PP/CNTs PNCs was studied by thermogravimetric analysis (TGA, Q500, TA Instruments). All samples were heated from 30 to 600 °C with a nitrogen flow rate of 60 mL/min and a heating rate of 10 °C/min. Differential scanning calorimeter (DSC, TA Instruments Q2000) measurements were implemented under a nitrogen flow rate of approximately 20 mL/min at a heating rate of 10 °C/min. The specimens were first heated from room temperature to 200 °C to remove the effect of previous thermal history and then cooled down to room temperature; after that the specimens were reheated again from room temperature to 200 °C.

Morphological Characterizations of the PP/CNTs Nanocomposites. The hot-pressed samples were broken in liquid nitrogen, and the morphology of the fracture surface of the samples was characterized with a field emission scanning electron microscope (SEM, JEOL JSM-6700F). The dispersion of the CNTs in the PNCs was studied by a transmission electron microscope (TEM, JEOL JEM-2010 FasTEM) with an accelerating voltage of 200 kV. The PP/CNTs nanocomposites were cut into thin strips and embedded into epoxy capsules, which were cured at 60 °C for 24 h. Then, the samples were microtomed into ca. 70 nm thick slices using an Ultra 45° diamond knife. The slices were deposited onto 400 mesh copper grids for imaging.

Optical Properties of PNCs. The UV−vis−NIR diffuse reflectance spectra (DRS) of the PP/CNTs PNCs were recorded on a JASCO spectrophotometer (model V-670) equipped with a Jasco ISN-723 diffuse reflectance accessory. The PP/CNTs samples used for the test were molded by hot pressing the composite powders at 120, 160, and 180 °C into a cylindrical shape with 25 mm in diameter and ∼2.0 mm in thickness.

Electrical Conductivity and Dielectric Permittivity Measurement. The electrical conductivity was measured following a standard four-probe method. To make sure that a precise voltage was applied on the two inner probes, V-source testing mode (Keithley 2400 source meter, USA) was introduced. The measured voltage was adjusted in the range from −1 to 1 V, and the corresponding current was measured and

DOI: 10.1021/am5082183
ACS Appl. Mater. Interfaces 2015, 7, 6125−6138

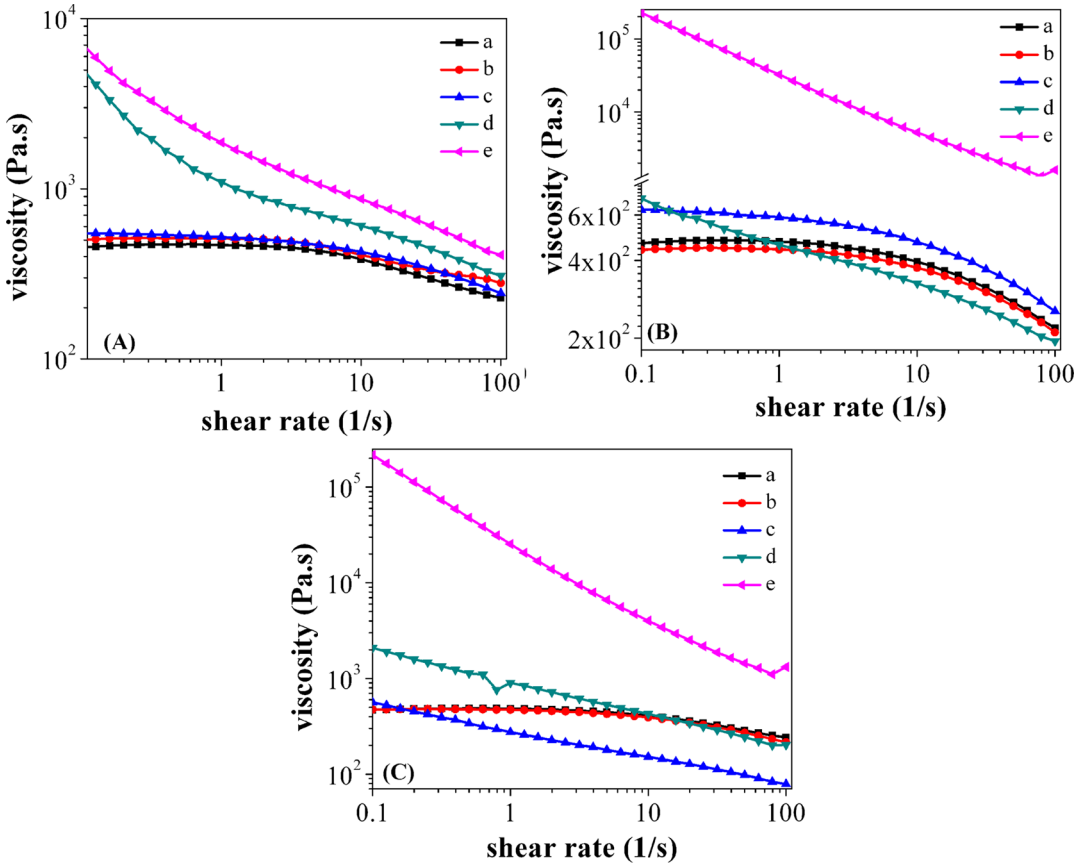

Figure 1. Viscosity vs shear rate of (a) melt pure PP and its PNCs with CNTs loading of (b) 0.1, (c) 0.3, (d) 1.6, and (e) 2.0 wt % processed at (A) 120, (B) 160, and (C) 180 °C.

recorded across the two outer probes. The dielectric permittivity was measured by a LCR meter (Agilent, E 4980A) equipped with a dielectric test fixture (Agilent, 16451B) at a frequency of 20−2 M Hz. A piece of rectangular standard Teflon sample with a permittivity of 2.1−2.4 was used for calibration before each test. The samples for both tests were prepared following the same procedures as that for the optical property test.

3. RESULTS AND DISCUSSION

3.1. Melt Rheological Behaviors of the PP/CNTs PNCs.

The rheological behaviors were tested for the melts at 200 °C of pure PP and its CNTs nanocomposites processed at different temperatures. Both Newtonian and shear-thinning behaviors were observed for the melts of pure PP and its PNCs. As shown in Figure 1, for pure PP, the first Newtonian plateau with a constant viscosity is clearly observed. The first Newtonian plateau of PP implies that in the test shear rate (lower than 5 s^{-1}) region the rebuilding of PP chain entanglement can follow the breaking rate of the physical cross-link sites.[35] However, with increasing shear rate, the rebuilding rate of the PP chain becomes lower than that of the physical cross-links broken,[35] the viscosity begins to sharply decrease, and the polymer melt enters a shear-thinning region. For pure PP, the shear-thinning region appears when the shear rate is increased higher than 5 s^{-1}. However, for the PNCs, the shear-thinning behavior can be observed with a much lower shear rate, 0.1 s^{-1}, for Figure 1B-d. The shift of the shear-thinning region to a lower shear rate range indicates that the CNTs favor the shear-thinning behavior of the PP/CNTs PNCs melts. The stronger shear-thinning behavior was also observed in other nanocomposites[36,37] such as layered double hydroxide/poly(ethylene terephthalate) and the nylon11/MWCNTs and was attributed to the orientation[38] and the network structure breakdown of the nanofillers.[39] Here, an increased pressing temperature leads to an improved dispersion of the CNTs in the PP matrix, and the CNTs network would be much easier to be destroyed; thus, in the samples prepared at a higher pressing temperature, the shear-thinning behavior was observed in a lower CNTs loading, Figure 1B and 1C.

It is worth noting that when the shear thinning happened the viscosity of certain PNCs (1.6 wt % for 160 °C and 0.3 wt % for 180 °C) was decreased even lower than that of pure PP. A decreased viscosity was also observed in the polymer nanosuspensions with nanoparticles.[11,40,41] This unique phenomenon was also observed by other researches, and two theories were developed to study the physics behind this reduced viscosity. One is the increased melt free volume resulting from the addition of nanoparticles in the entangled and confined systems ($h < R_g$, h is the average interparticle half-gap; R_g is the polymer radius of gyration),[42,43] and the other is the dilution effect of nanoparticles, which provides a constraint release of polymer chain entanglement.[42] However, unlike certain PNCs systems such as the PP/alginate suspensions with a lower viscosity than that of bulk material in the whole test frequency range,[44] the viscosity in the PP/CNTs system is higher than that of pure PP in the low shear rate range and becomes lower than that of pure PP at higher shear rate (1.0 and 0.2 s^{-1} for Figure 1B-d and 1C-c, respectively). A similar phenomenon was also observed in the study of long chain branching and linear material such as the metallocene

DOI: 10.1021/am5082183
ACS Appl. Mater. Interfaces 2015, 7, 6125−6138

polyethlenes with different long chain branching densities.[45] Though the nanoparticles are reported to promote the orientation of polymer chains,[46] limited report can be found on its mechanism. In the long chain branching material, the rheological behavior would largely depend on the reptation (a process by which a given chain crawls along the primitive path defined by topological constrains due to the other chains in the melt)[47] and the restraint of branches on the motion of backbone would lead to an extensional force on the backbone, which would further enhance the disentanglement of the polymer chains and caused a dramatically decreased viscosity.[48] Thus, in the PP/CNTs system, due to the interaction between nanofillers and polymer matrix, the CNTs could serve as the branch of the polymer chains, which enhances the disentanglement[49] under the shear field and causes a reduced viscosity, Scheme 1.

Scheme 1. Nanoparticles Act as Branches of the PP Polymer Chain Leading to an Extensional Force on the Backbone

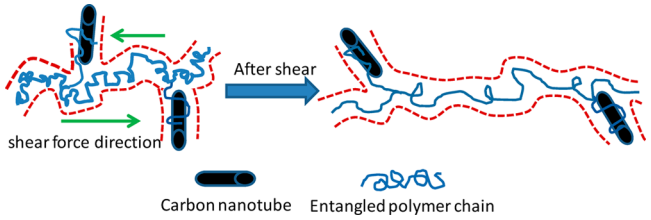

In addition, the storage modulus (G'), loss modulus (G''), and loss factor (tan δ) of the PP/CNTs nanocomposites were also studied, Figure 2. Both G' and G'' increase with increasing the CNTs loading in the low-frequency range, which is also observed in the polylactide/layered silicate nanocomposite[50] and attributed to the enhanced solid-like behavior of the PNCs introduced by the nanofillers.[51] The tendency of solid-like behavior of PNCs was also observed by the study of the tan δ vs ω curve. As shown in Figure 2C, with increasing the CNTs loading, the peak of tan δ shifts to a higher value. A switch from positive to negative for the slope of tan δ indicates the transition of materials from solid-like to melt-like behavior.[52] Thus, the peak shift of tan δ also indicates the improvement of solid-like behavior of the PNCs. In addition, at low frequency, the "plateau" area is observed in both G' and G'', where the G' and G'' values were less dependent on the frequency. The existence of the "plateau" area indicates the interactions between the nanoparticles and the polymer matrix.[53] Moreover, the value of tan δ in PP was observed to be higher than that of PNCs; the increased tan δ was attributed to the stronger interaction between the PP molecules and the CNTs than that among the PP molecules, which leads to more friction heat loss in pure PP than that of PNCs.[54]

3.2. Crystalline Structure. The effects of processing temperature on the crystal structure of pure PP and its PNCs with 2.0 wt % CNTs were studied by XRD. As shown in Figure 3, for both pure PP and its PNCs prepared at 120 °C, the intensity of the first peak (110) is stronger than that of the second one (040), which is a typical XRD pattern of the α

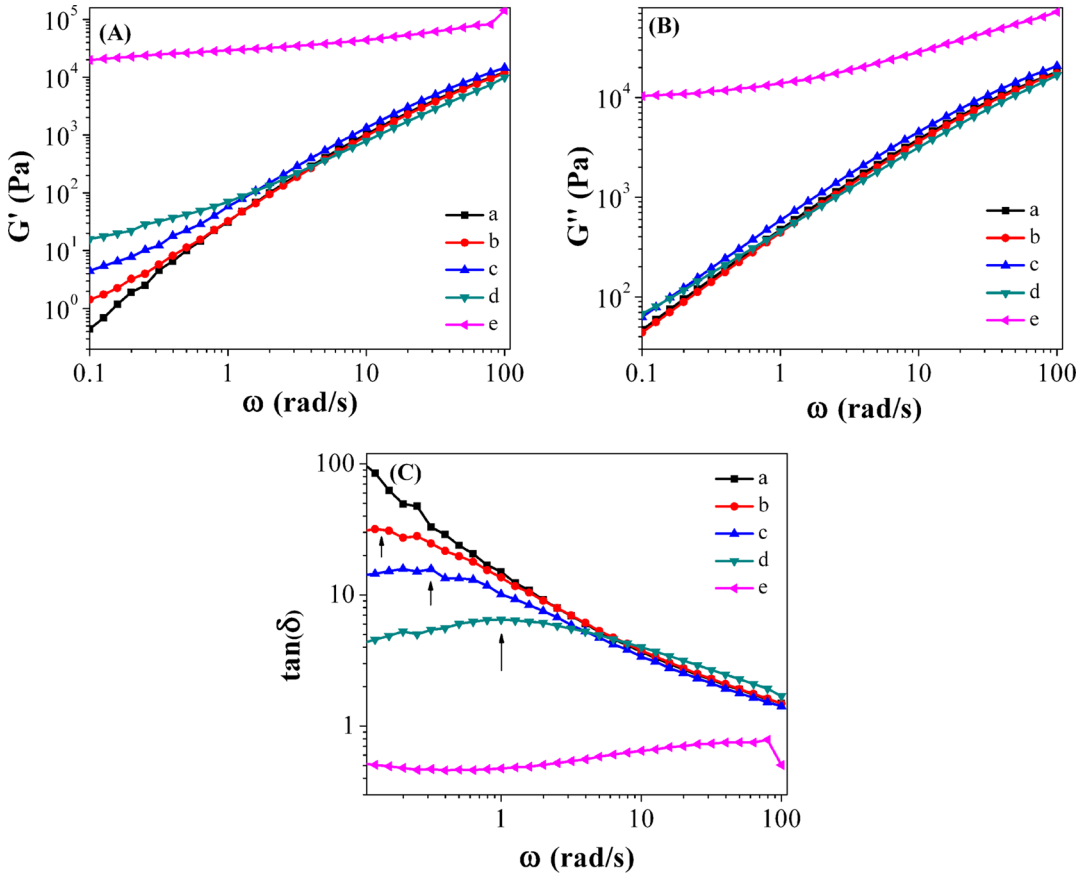

Figure 2. (A) Storage modulus (G'), (B) loss modulus (G''), and (C) loss factor (tan δ) vs angular frequency (ω) of (a) pure PP and its PNCs with CNTs loading of (b) 0.1, (c) 0.3, (d) 1.6, and (e) 2.0 wt % processed at 160 °C.

DOI: 10.1021/am5082183
ACS Appl. Mater. Interfaces 2015, 7, 6125−6138

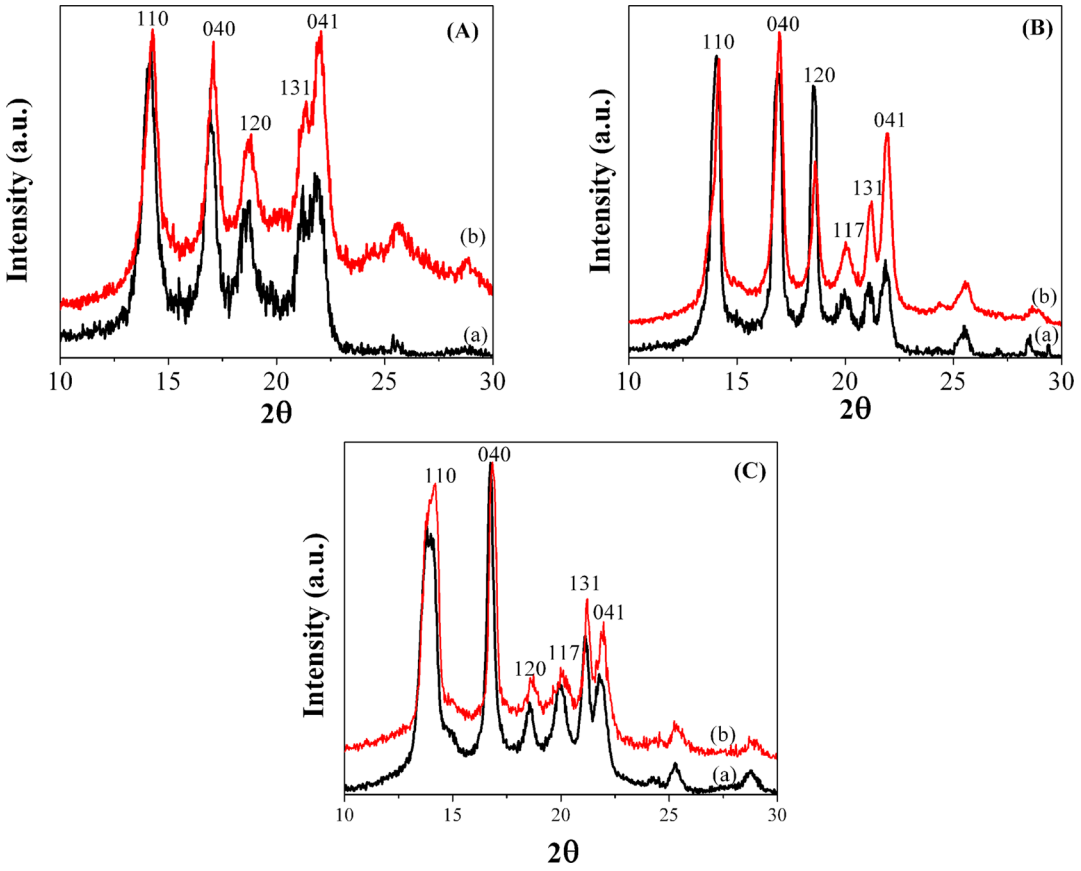

Figure 3. X-ray diffraction patterns of (a) pure PP and (b) its PNCs with 2.0 wt % CNTs processed at (A) 120, (B) 160, and (C) 180 °C.

phase PP.[53] The introduction of CNTs causes no crystal variation of the PP resin for this temperature, Figure 3A. However, when the temperature increased to 160 and 180 °C, the characteristic peak of the γ phase at 2θ = 20.07°[53] was observed in both pure PP and its PNCs, Figure 3B and 3C. Meanwhile, the peak intensity at 2θ = 18.50°,[53] the distinctive peak of α-phase PP, is decreased, Figure 3B and 3C. In order to explore the influence of CNTs on the crystalline phase of PP, the amount of γ-phase PP (X_γ) is calculated by eq 1[55]

$$X_\gamma = h_\gamma/(h_\gamma + h_\alpha) \quad (1)$$

where h_γ and h_α are the peak height at 2θ = 20.07° and 18.5° for the (117) and (120) peak, respectively. The value of X_γ was summarized in Table 1; it can be observed that compared with pure PP, the PNCs with 2.0 wt % CNT exhibit more γ-phase PP, indicating that the CNTs promoted the γ-phase PP formation. In addition, it is shown that for both pure PP and its PNCs the percentage of γ-phase PP increased with increasing processing temperature and the γ-phase PP became the dominant phase for the PNCs processed at 180 °C. The variation of the crystal structure was attributed to the higher crystallized temperature, which favors γ-phase PP formation.[56] The same phenomenon was also observed in the PNCs with 0.1, 0.3, and 1.6 wt % CNTs prepared at different temperatures (Table S1, Supporting Information).

Table 1. Amount of γ-Phase PP of Pure PP and Its PNCs with CNTs

samples	120 °C	160 °C	180 °C
pure PP	0	0.1168	0.5770
2.0 wt % CNTs	0	0.2533	0.6276

3.3. Thermogravimetric Analysis of PP and Its Nanocomposites. The thermal decomposition curves of pure PP and its CNTs PNCs are shown in Figure 4. For all samples, there is a sharp weight loss stage in the temperature range from 350 to 500 °C, which is caused by the chain breakdown of the polymer structure. From the onset decomposition temperature (T_{1onset}) summarized in Table 2, introduction of CNTs caused no obvious difference on the T_{1onset} value. However, when carefully studying the DTG curves, an extra peak can be observed for all PNCs between 300 and 400 °C, Figure 4B, and no peak is shown in the same range for both pure PP and pure CNTs, indicating that a new weight loss stage of the PNCs was introduced by the interaction between CNTs and PP. The onset decomposition temperature (T_{2onset}) of the weight loss stage from 300 to 400 °C was also summarized in Table 2. The T_{2onset} value was almost the same for all PNCs and did not change with increasing the CNTs loading. This unique decomposition behavior of the PP/CNTs PNCs in the low-temperature range is probably due to the wrapped xylene in the PP matrix.[57] Compared with pure PP sample, it becomes more difficult to completely remove xylene in the PNCs due to the physical barrier effect of CNTs.

3.4. Differential Scanning Calorimetry (DSC) of PP and Its Nanocomposites. The crystallization and melting processes of pure PP and its PNCs were studied by the DSC test, Figure 5. The crystallization process can be observed in the DSC curve, and the crystallization temperature (T_c) is summarized in Table 3; the value of T_c first increases with increasing CNT loading and then decreases with further

DOI: 10.1021/am5082183
ACS Appl. Mater. Interfaces 2015, 7, 6125−6138

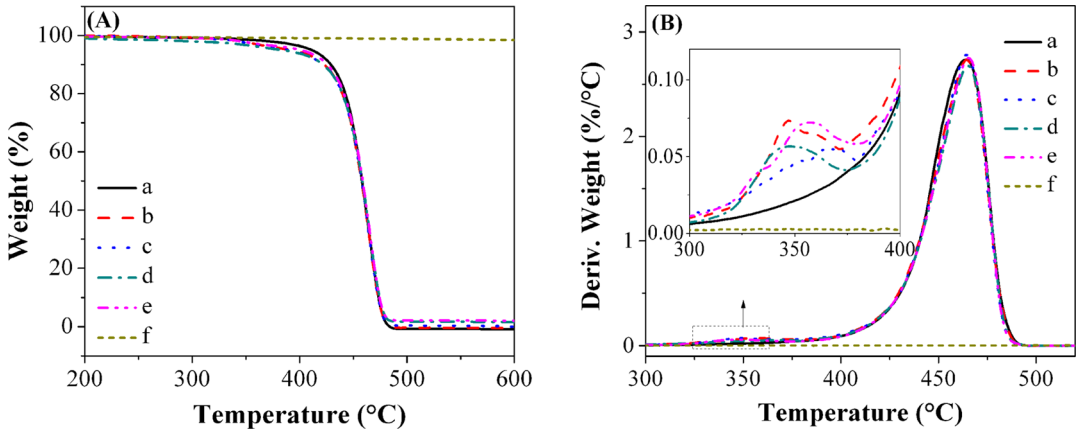

Figure 4. (A) Thermogravimetric analysis (TGA) curves and (B) derivative thermogravimetric (DTG) curve of (a) pure PP and its PNCs with CNTs loading of (b) 0.1, (c) 0.3, (d) 1.6, and (e) 2.0 wt % and (f) pure CNTs.

Table 2. Onset Temperature T_{1onset} and T_{2onset} of the Pure PP and Its PNCs with CNTs

samples	T_{1onset} (°C)	T_{2onset} (°C)
pure PP	439.87	N/A
0.1 wt % CNTs	439.47	324.77
0.3 wt % CNTs	440.16	325.78
1.6 wt % CNTs	440.65	324.75
2.0 wt % CNTs	440.87	326.67

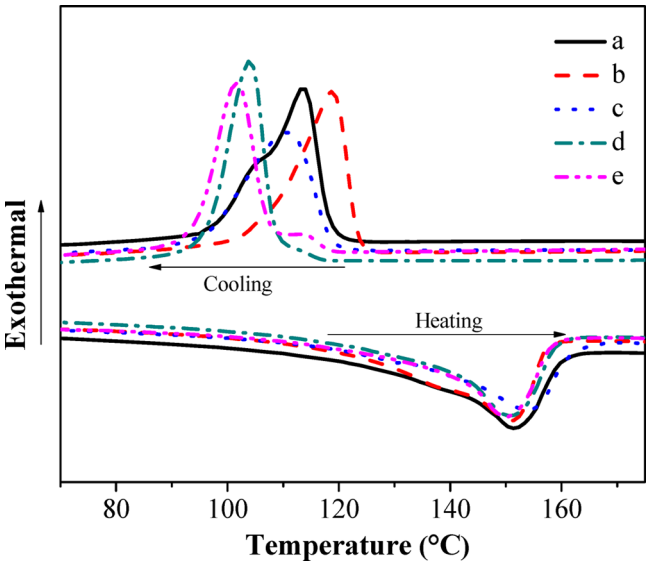

Figure 5. DSC curves of pure (a) pure PP and its PNCs with CNTs loading of (b) 0.1, (c) 0.3, (d) 1.6, and (e) 2.0 wt %.

Table 3. DSC Characteristics of pure PP and its PNCs with CNTs

loading of CNTs	T_c (°C)	ΔH_c (J g^{-1})	T_m (°C)	ΔH_m (J g^{-1})	F_c (%)
pure PP	113.55	88.32	151.55	99.38	47.55
0.1 wt % CNTs	118.64	86.19	150.80	94.35	45.19
0.3 wt % CNTs	111.45	82.68	153.46	86.58	41.55
1.6 wt % CNTs	103.89	82.96	150.94	86.89	41.99
2.0 wt % CNTs	101.59	77.41	149.82	85.06	41.36

increasing the CNTs loading. The variation of T_c can be attributed to different functions of the CNTs during crystallization of PP. The spherulitic growth rate (G) of the polymer crystallization can be expressed by eq 2[58−60]

$$G = G_0 \exp\left[\frac{-U^*}{R(T_c - T_0)}\right]\exp\left[\frac{-K_g}{(T_c \Delta T f)}\right] \quad (2)$$

where G_0 is the pre-exponential factor, U^* is the activation energy for transportation of polymer chain segments to the crystallization sites, R is the gas constant, $\Delta T = T_m^0 - T_c$, where T_m^0 is the equilibrium T_m and T_c is the crystallization temperature, f is the factor representing the decrease in heat of fusion with decreasing temperature, T_0 is the hypothetical temperature, where all motions associated with viscous flow are prohibited, and usually taken 30 K below the glass transition temperature,[61] and K_g is the nucleation constant, which can be calculated based on eq 3[59]

$$K_g = \frac{4EE_e b_0 T_m^0}{\Delta H_f k_B} \quad (3)$$

where E and E_e are side and fold surface free energies that represent the work required to create a new surface, b_0 is the single-layer thickness, ΔH_f is the enthalpy of melting, and k_B is the Boltzmann constant.

As shown in eq 2, crystallization formation is determined by two parts: the first part $-U^*/R(T_c - T_0)$ describes the transport of polymer chain segments to the growth front (where polymer chains were simultaneously adsorbed and crystallographically attached to the nucleation),[62] and the second part $-K_g/(T_c \Delta T f)$ is attributed to the nucleation process. The CNTs were reported to be serving as nucleation sites of PP,[63] and the nucleation site could promote the crystallization by reducing the surface free energy barrier (E, E_e) toward nucleation;[64] thus, for the PNCs with a lower loading (0.1 wt %) of CNTs, the crystallization of PP was initiated at a higher temperature than that of pure PP, Figure 5. However, with increasing the loading of CNTs, even the increment is small, since the CNTs are not uniformly dispersed in the PP matrix, the nanofillers could easily agglomerate and would constrain the movement of polymer chains to the growth front, leading to a higher U^* value and causing the crystallization temperature to shift to a lower value, which was also observed in the Fe@Fe_2O_3/PP PNCs.[53]

In addition, it is worth noting that a small shoulder observed in the PNCs with 2.0 wt % CNTs, in the cooling procedure,

DOI: 10.1021/am5082183
ACS Appl. Mater. Interfaces 2015, 7, 6125−6138

when the temperature decreased the shoulder was formed first and then the main crystallization peak was observed at a lower temperature range, Figure 5e. The same phenomenon was also observed in the PNCs with 2.0 wt % CNTs prepared at different temperatures (Figure S2, Supporting Information); however, for pure PP, no shoulder was observed during the crystallization process (Figure S3, Supporting Information). It is known that the separation of the crystallization peak indicates a variation of the crystal structure. For pure PP with both α and γ phases formed during crystallization, γ phase would first form dominant lamellae and the α phase would grow on it with cooling proceeding.[65] Thus, the small shoulder observed in the cooling procedure can be attributed to the formation of γ-phase PP; when the temperature further decreased, the α-phase PP would grow on the γ-phase PP and the main crystallization peak was observed. Thus, the extra shoulder shown in the PNCs indicated that the CNTs promote the γ-phase PP, consistent with the XRD study.

For the second heating process, the melting peak was shown; the peak temperatures (T_m) are summarized in Table 3; the T_m of the PNCs was observed to be almost the same as that of pure PP. Both the enthalpy of fusion (ΔH_m) and the enthalpy of crystallization (ΔH_c) are also summarized in Table 3. For all samples, the value of ΔH_m was larger than ΔH_c, which was caused by the recrystallization of the samples; the crystalline fraction (F_c) of pure PP and its PNCs is calculated from eq 4[66]

$$F_c = \frac{\Delta H_m}{\Delta H_m^0 f_p} \quad (4)$$

where ΔH_m is the enthalpy of the samples, ΔH_m^0 is the enthalpy for a theoretically 100% crystalline PP (209 J/g),[53] and f_p is the weight fraction of the polymer. From the results summarized in Table 3, it can be observed that the PNCs show a lower F_c than pure PP, which can be attributed to the disturbing effect of nanofillers during the formation of crystalline structure of PP polymer chains.[53]

3.5. Electrical Conductivity (σ) of PP/CNTs Nanocomposites. The conductivity of the PNCs as a function of the CNT loading at different processing temperatures is shown in Figure 6. The conductivity (~1 × 10^{-9} S/cm) of pure PP was from the literature.[67] The conductivity is observed to increase with increasing CNT loading, and the PNCs with 2.0 wt % CNTs and prepared at 120 °C exhibit the highest conductivity of 0.16 S/cm, which is 4 orders of magnitude higher than that of the PP/CNTs PNCs even with 5 wt % CNTs prepared by dispersing the CNTs in the PP matrix.[68] The outstanding electric conductivity was attributed to the unique network formation of CNTs in PP. At 120 °C, PP just began to melt; when the fabricated PP powders coated with CNTs were pressed, the powders would only change shape without breaking the coating layer of CNTs, in which condition the CNTs would be pressed together, Scheme 2. The morphology of the PNCs was studied, Figures 7 and 8. For the PNCs prepared at 120 °C, the surface of the deformed powders with a CNTs coating can be observed, Figure 7A, and the CNTs agglomerate together to form the network structures, Figure 8A and 8C. With the formed CNTs network structure, the electrons may be able to hop from a nanotube to an adjacent one, which leads to the conductivity increased.[69−71] To explore the electron transportation mechanism of the

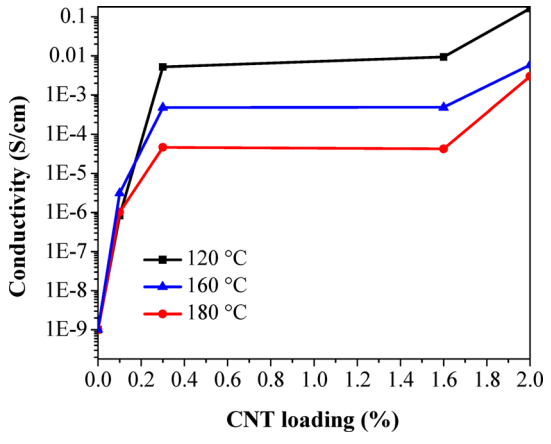

Figure 6. Electrical conductivity of PNCs vs CNT loading for the samples processed at (a) 120, (b) 160, and (c) 180 °C.

Scheme 2. Morphology of PNCs with CNTs at Different Processing Temperatures

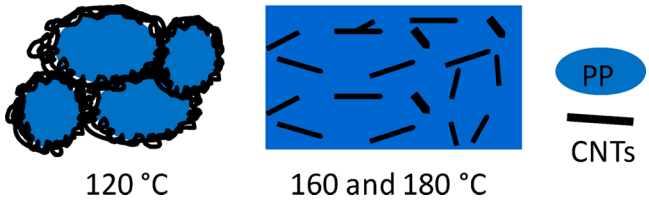

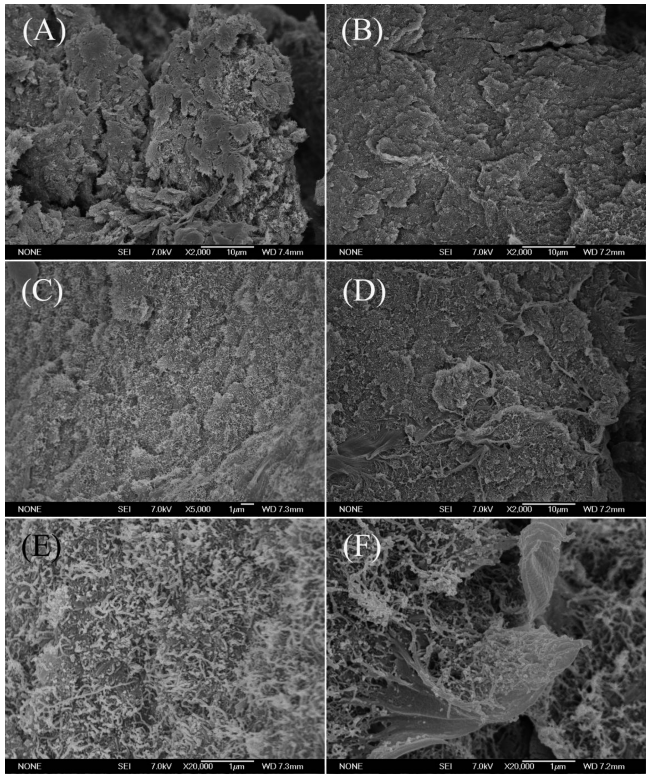

Figure 7. SEM microstructures of PNCs with 2.0 wt % CNTs prepared at (A) 120 and (B) 180 °C; PNCs with 0.3 wt % prepared at (C, E) 160 and (D, F) 180 °C.

DOI: 10.1021/am5082183
ACS Appl. Mater. Interfaces 2015, 7, 6125−6138

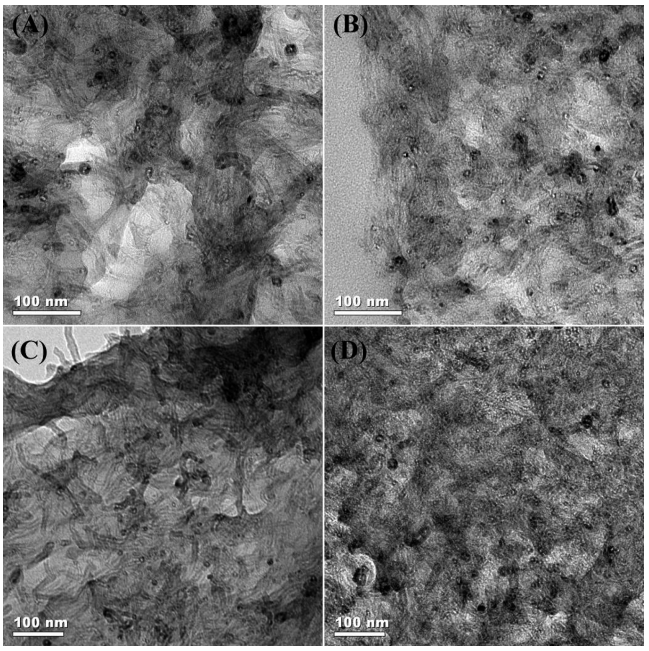

Figure 8. TEM microstructures of the PNCs with 0.3 and 2.0 wt % CNTs prepared at (A, C) 120 and (B, D) 180 °C, respectively.

PNCs, the relationship between temperature and σ was investigated by using eq 5[72]

$$\sigma = \sigma_0 \exp\left[-\left(\frac{T_0}{T}\right)^{1/n}\right] \quad (5)$$

where T_0 is the characteristic Mott temperature related to the electronic wave function localization degree, σ_0 is the conductivity at infinite high temperature, and n can be equal to 2, 3, and 4, which represent one-, two-, and three-dimensional systems, respectively. The obtained T_0 and σ_0 values for each sample are summarized in Table 4. σ_0 increased with increasing loading of CNTs. Within a certain CNTs loading, the σ_0 value of the composites is decreased with increasing processing temperature. The T_0 value increases with decreasing loading of CNTs. Within a certain CNTs loading, the T_0 of the composites is increased with increasing processing temperature. It is known that a higher T_0 indicates a stronger localization of the charge carriers and thus represents a lower σ.[73] The variation of the σ_0 and T_0 values is associated with the electrical conductivity mechanism of the composites. As shown in Figure 9A, the conductivity of the PNCs decreases with increasing temperature, and in Figure 9B, n is equal to 4 best fit for samples, indicating a 3-d VRH behavior. The electrical conductivity mechanism implied that the conductivity of the PNCs follows the electron theory, which depends on the network structure in the polymer matrix. For the PNCs prepared at 160 and 180 °C, since the matrix was melted, the surface became flatter and the CNTs coating layer was separated by PP, Figure 7F; the PP can limit the charge transportation and cause a higher T_0 and lower σ_0. The CNTs were observed dispersing among the PP matrix to build the network structure, Figure 8B and 8D. The network structure was observed with only 0.3 wt % CNTs in PNCs prepared under both high (180 °C) and low (120 °C) temperatures, indicating the low percolation concentrations for all PNCs.[74] However, the network density is different. It is known that the conducting path was attributed from the CNTs and at higher temperatures (160 and 180 °C); since the CNTs are dispersed in PP matrix, limited CNTs can join in the conductive paths formation.[75] However, for the PNCs prepared at low temperature (120 °C), as the CNTs agglomerated to form the bundles, the network density increases. More CNTs get involved in forming the conductive network and lead to a lower T_0 and higher electrical conductivity.[75]

Table 4. T_0 and σ_0 for PP/CNTs PNCs

samples	$T_0 \times 10^5$ (°C)	σ_0 (s/cm)
2.0 wt % CNTs-120 °C	11.36	28 488 185
2.0 wt % CNTs-160 °C	65.00	272 665
0.3 wt % CNTs-120 °C	290.70	85 819
0.3 wt % CNTs-180 °C	420.42	578.25

In addition, the obtained T_0 and σ_0 values for each sample are summarized in Table 4. The variation of σ_0 value corresponds with the conductivity value in Figure 9A; σ_0 increased with increasing loading of CNTs, and at same loading, the σ_0 value depends on the processing temperature. T_0 increases, and a higher T_0 indicates a stronger localization of the charge carriers and thus represents a lower σ.

3.6. Optical Property of PP/CNTs Nanocomposites. The optical property of pure CNTs and its PNCs was studied by ultraviolet−visible (UV−vis) spectroscopy, Figure 10. From the UV−vis absorbance spectra, the photonic energy band gap (E_g) value of the CNTs can be obtained from the Tauc plot,[76] which describes the $\alpha h\upsilon$ value as a function of photon energy ($h\upsilon$)

$$\alpha h\upsilon = (h\upsilon - E_g)^n \quad (6)$$

where α, h, and υ are the absorbance coefficient, Planck's constant, and the photon frequency, respectively. The Tauc plot was converted from the diffuse reflectance UV−vis spectra. The parameter n is a pure number associated with the type of electronic transitions. n is 1/2 for the direct-allowed (characterized by the minimum energy level of the lowest conduction band positioned in k space directly under the maximum of the highest valence band) and 2 for the indirect-allowed (instead of directly under the maximum of the highest valence band, the minimum energy level of the lowest conduction band is shifted relative to the maximum of the highest valence band in k space).[77,78] The value of n is reported to be 2[79] for the CNTs, and the band gap value is obtained by extrapolation of the linear portion of the curve to the energy axis. The band gap of pure CNTs is found to be 1.50 eV, Figure 10B, which is pretty close to the reported 1.543 eV for the transition between the second pair of van Hove singularity at above and below the Fermi level of CNTs with the assignment of (9,8).[80]

The band gap (E_g^{opt}) values of pure CNTs and its CNTs PNCs can be observed in Figure 10B and 10D. The E_g^{opt} of all the PNCs is higher than that of pure CNTs and decreases with increasing CNT loading. At the same loading of CNTs, the E_g^{opt} of the nanocomposites depends on the processing temperature. The variation of E_g^{opt} can be attributed to the strain of CNTs,[81] which was introduced during the hot-pressing process.

It is known that the band gap of CNTs depends on the diameter[82] and chirality, which could vary with the applied strain.[81] For CNTs, its chirality is defined by the tube index (m,n). The armchair metallic CNTs ($m = n$), which are of high symmetry, are less sensitive to the tensile strain than the

DOI: 10.1021/am5082183
ACS Appl. Mater. Interfaces 2015, 7, 6125−6138

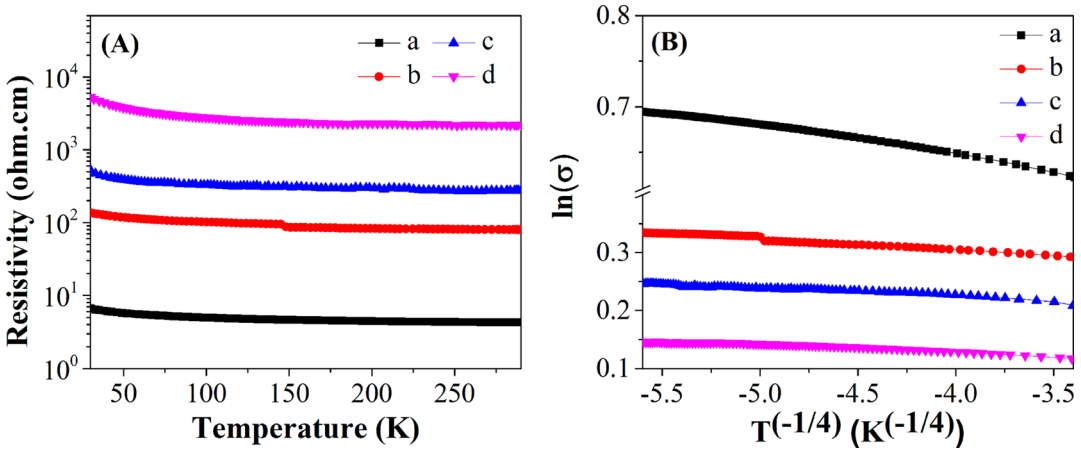

Figure 9. (A) Resistivity vs temperature and (B) $\ln(\sigma)$ vs $T^{-1/4}$ of (a and b) PNCs with 2.0 wt % CNTs processed at 120 and 160 °C and (c and d) PNCs with 0.3 wt % CNTs processed at 120 and 180 °C.

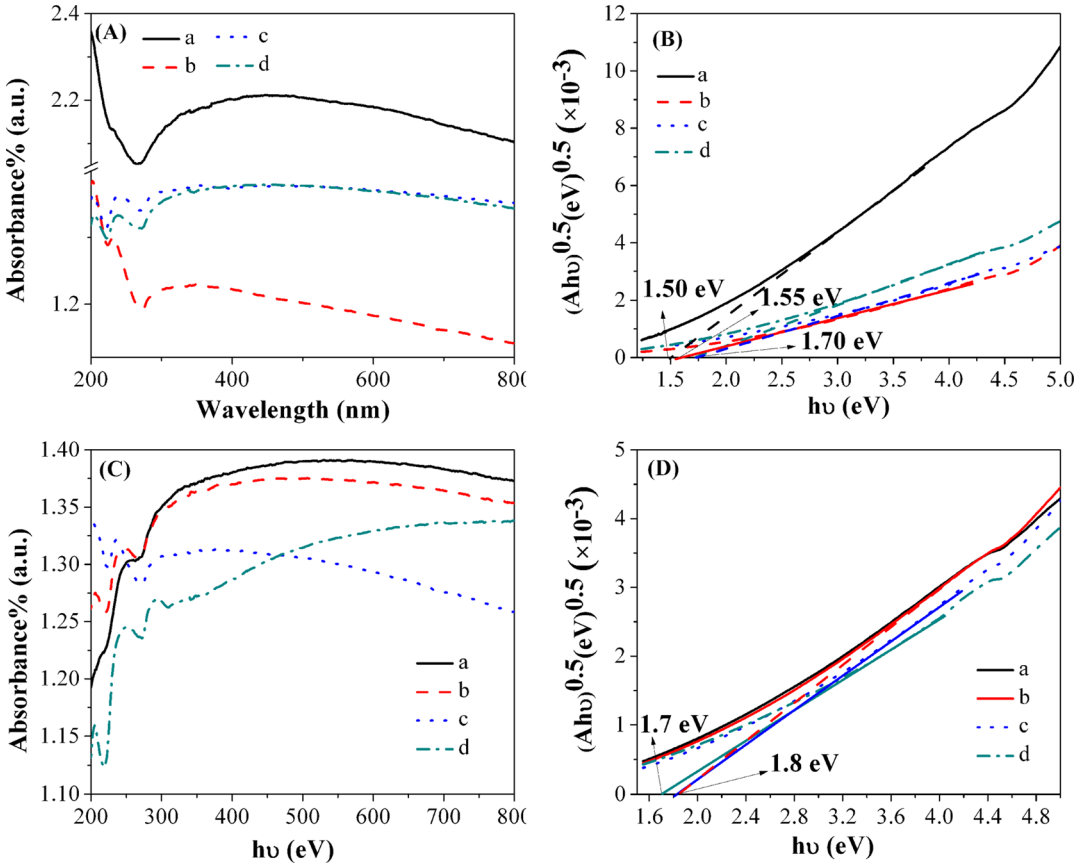

Figure 10. (A and C) UV−vis absorbance spectra and (B and D) converted from diffuse reflectance spectra data of (A and B) (a) pure CNTs and PNCs with 2.0 wt % CNTs processed at (b) 120, (c) 160, and (d) 180 °C and (C and D) PNCs with the CNTs loading of (a) 0.1, (b) 0.3, (c) 1.6, and (d) 2.0 wt %, processed at 160 °C.

semiconducting CNTs ($m - n \neq 3N$, N is an integer) with lower symmetries. The effect of strain on the band gap of CNTs is complicated. The strain on CNTs can play a positive or negative effect on the electrical property of CNTs. It is observed that the uniaxial or torsional strain could cause the insulator−metal transition of the SMNTs, due to the change of quantum number.[83,84] However, for graphene, uniaxial strain caused the red shift of the 2D and G bands, and the shift was studied with the elongation of the carbon−carbon bonds, which would weaken the bonds and lead to a decreased vibrational frequency.[85] For the PNCs, the shift of the band gap was also observed in the poly(methyl methacrylate) (PMMA)/CNTs system, the effects of load transfer, strain, and interfacial adhesion were studied, and the peak splitting observed in a higher strain (0.8%) was attributed to the slip of nanotubes in the polymer matrix.[86] For the PP/CNTs system, a lower E_g^{opt} value, Figure 10B, was observed in the samples prepared at 160 and 180 °C, at which temperature PP was already melted and the stronger deformation of polymer matrix would cause more strain on the CNTs. In addition, the changing trend of E_g^{opt}

DOI: 10.1021/am5082183
ACS Appl. Mater. Interfaces 2015, 7, 6125−6138

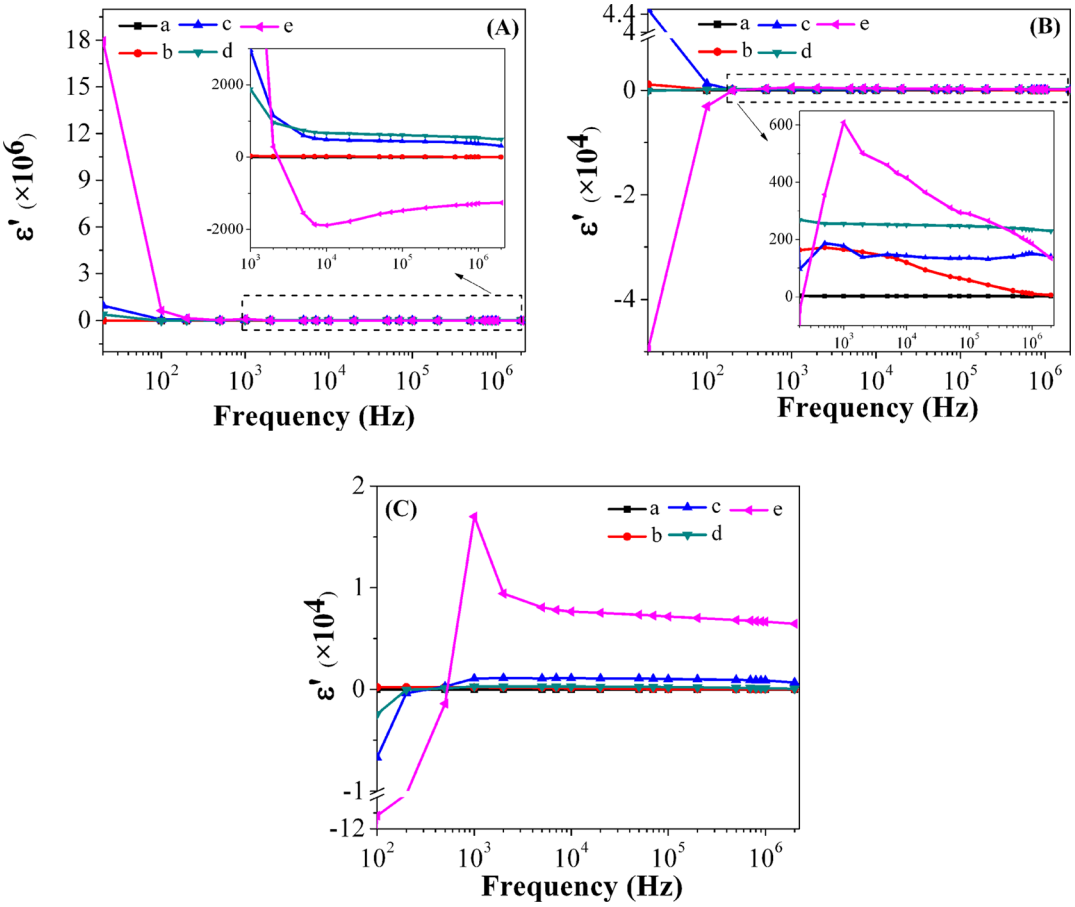

Figure 11. Real permittivity (ε') of (a) pure PP and its PNCs with the CNTs loading of (b) 0.1, (c) 0.3, (d) 1.6, and (e) 2.0 wt % processed at (A) 120, (B) 160, and (C) 180 °C.

value of the PNCs is consistent with the electrical conductivity of the PNCs; the PNCs with higher conductivity exhibit a lower E_g^{opt}.

3.7. Dielectric Permittivity. For the dielectric property study, the effects of processing temperature on the real permittivity (ε') of pure PP and its PNCs are shown in Figure 11. It is worth noting that the PNCs with 2.0 wt % CNTs processed at three different temperatures all exhibit processing temperature-dependent negative ε' over the testing frequency range. The negative ε' is widely observed in the CNTs and attributed to the metallic nature of the CNTs.[27] However, the switching frequency from positive to negative depends on the composite sample pressing temperature. For the PNCs prepared at 120 °C, the negative ε' is observed at a frequency higher than 2000 Hz. However, the negative ε' is observed in the frequency range below 1000 Hz for the samples processed at 160 and 180 °C. In addition, it is worth noting that the variation tendency of the permittivity as a function of the frequency for the PNCs pressed at 120 °C (changing from a positive to a negative value with increasing frequency, Figure 11A) is in symmetry with that of PNCs pressed at 160 and 180 °C (changing from a negative to a positive value with increasing frequency, Figure 11B and 11C).

The formation of the symmetric ε' variation trend was further explored by studying the relationship between the negative permittivity and the plasma frequency (ω_p). Negative permittivity observed in the metal-based negative refractive index materials[25] was attributed to the plasma-like resonance of free electrons on the metal surface.[26] The permittivity as a functional of ω_p was studied by the Drude model, eq 7[31]

$$\varepsilon^*(\omega) = 1 - \frac{\omega_p^2}{\omega(\omega + i\gamma)} \tag{7}$$

where $\omega_p \equiv (Ne^2/\varepsilon_0 m)^{1/2} = (4\pi Ne^2/m^*)$ is the plasma frequency, m^* is the effective mass, γ stands for the damping constant, ε_0 is the vacuum permittivity, N represents the charge carrier density, and ω is the angular frequency.[87] In order to fit the infrared optical data on the metals, the frequency-dependent relaxation time is introduced to modify the Drude model (eq 7) to eq 8[88,89]

$$\begin{aligned}\varepsilon^*(\omega) &= 1 - \frac{\omega_p^2}{\omega(\omega + i\gamma)} \\ &= 1 - \frac{\omega_p^2}{\omega(\omega + i/\tau)} \\ &= \left(1 - \frac{\omega_p^2\tau^2}{1 + \omega^2\tau^2}\right) + i\left(\frac{\omega_p^2\tau}{\omega(1 + \omega^2\tau^2)}\right)\end{aligned} \tag{8}$$

where τ is the relaxation time and $\tau = 1/\gamma$. From eq 8, negative permittivity is expected when the frequency is below the ω_p, and the permittivity becomes positive when the frequency is above the ω_p.[90] On the basis of the Drude model, the ω_p values for the PNCs with 2.0 wt % CNTs processed at 160 and 180 °C should be between 200 and 1000 Hz considering the

DOI: 10.1021/am5082183
ACS Appl. Mater. Interfaces 2015, 7, 6125−6138

observed negative ε' at 200 Hz (below the ω_p) and positive ε' at 1000 Hz (above the ω_p), Figure 11B and 11C. However, for the PNCs processed at 120 °C, Figure 11A, ε' showed a positive value at a lower frequency and was decreased to a negative value with increasing the frequency, which could not be described by the Drude model. The same phenomenon was also observed in polypyrrole (PPy),[91] with the negative permittivity in the frequencies below the first ω_p changing to positive with frequencies above the first ω_p, ε' was decreased from positive to negative again with further increasing the frequency, and ε' turned from negative to positive once more at the second ω_p. The first ω_p was claimed to be attributed to the most delocalized electrons, and the second ω_p originated from the confined electrons.[91] In the study of negative permittivity in the metal materials, it was found that at wavelengths shorter than 550 nm the Drude model was not accurate to describe the value of permittivity. In the low-frequency range, the positive ε' would decrease and even turn to negative with increasing test frequency. With further increasing the frequency, the variation of ε' would follow the Drude model.[92] This unique variation of ε' as a function of frequency was known as interband transition, as shown in Scheme 3. This interband transition can be attributed to the higher energy photons promoting electrons of lower lying bands to the conduction band.[92] When considering the interband transition, the Drude model can be written as eq 9[92]

Scheme 3. Contribution of Interband Transition to the Real Permittivity as a Function of Frequency

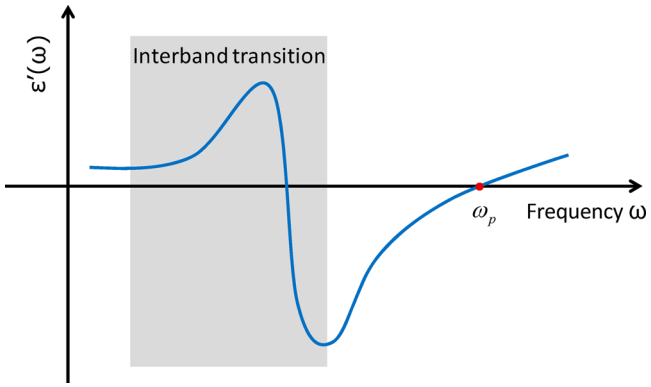

$$\varepsilon_{\text{interband}}^{*}(\omega) = 1 + \frac{\omega_p^2(\omega_0^2 - \omega^2)\tau^2}{\omega^2 + (\omega_0^2 - \omega^2)\tau^2} + i\frac{\omega_p^2\omega\tau}{\omega^2 + \tau^2(\omega_0^2 - \omega^2)^2} \quad (9)$$

The interband transition has been observed in the 2D graphene[93] and the PNCs with carbon nanofillers,[94] where the second frequency for the variation of ε' from negative to positive was considered as ω_p.[94] Here, for the PNCs with 2.0 wt % CNTs processed at 120 °C, Figure 11A, the interband transition of ε' was observed to take place in a low-frequency range (between 2000 and 5000 Hz); however, the ω_p for the variation of ε' from negative to positive was not observed. The lack of ω_p in the test frequency range was associated with the CNTs network structure formed in the PNCs processed at 120 °C. It is known that the value of the ω_p depends on the 3-d network of the nanofiller in the polymer matrix.[94] After being dispersed in the polymer substrate, dilution of the metallic wires would lead to a reduced density of the active electrons and thus the ω_p shifted to a lower frequency range.[31] A similar phenomenon was also reported in the graphene nanocomposite systems, where ω_p was observed to depend on the carrier density in graphene.[95] For the PNCs processed at 120 °C, the good network of CNTs would lead to a high ω_p value, which exceeded the testing frequency range; thus, no ω_p was observed, Figure 11A. In addition, since ω_p depends on the charge carrier density, the higher ω_p value of the PNCs processed at 120 °C indicates a higher charge carrier density, i.e., a higher electrical conductivity. This observed dielectric permittivity variation as a function of processing temperature is in good agreement with the electrical conductivity study, in which the electrical conductivity of the PNCs processed at 120 °C is observed higher than that of PNCs processed at 160 and 180 °C.

4. CONCLUSIONS

The CNTs coated on the surface of gelated/swollen soft PP powders were easily pressed together and formed a network structure in the hosting materials, which led to the outstanding electrical properties. Meanwhile, the CNTs were observed to favor the formation of γ-phase PP. The CNTs served as nucleating sites to promote crystallization of PP at the lower loading (0.1 wt %). CNTs also served as the branches of polymer chains to enhance the disentanglement of polymer chains and caused a decreased viscosity of PNCs even lower than that of pure PP. For the PP/CNTs system, the lower band gap of CNTs was associated with the stronger deformation of polymer matrix at elevated processing temperatures. Finally, ω_p, which is proportional to the charge carrier density, was studied with the negative real permittivity observed in the PNCs. For the PNCs processed at 120 °C, the good network of CNTs led to a high ω_p value and indicated a higher charge carrier density.

■ ASSOCIATED CONTENT

Supporting Information

Amount of γ-phase PP in the PNCs with 0.1, 0.3, and 1.6 wt % CNTs; DSC curves of pure PP and its PNC with 2.0 wt % CNTs prepared at different temperatures. This material is available free of charge via the Internet at http://pubs.acs.org.

■ AUTHOR INFORMATION

Corresponding Authors

*E-mail: suying.wei@lamar.edu. Phone: 409-880-7976.
*E-mail: zguo10@utk.edu. Phone: 865-974-2933.

Notes

The authors declare no competing financial interest.

■ ACKNOWLEDGMENTS

This project was supported by the National Science Foundation (CMMI 10-30755) and American Chemical Society Petroleum Research Fund (ACS PRF# 53930-ND6). S.W. acknowledges the Welch Foundation (V-0004).

■ REFERENCES

(1) Stankovich, S.; Dikin, D. A.; Dommett, G. H. B.; Kohlhaas, K. M.; Zimney, E. J.; Stach, E. A.; Piner, R. D.; Nguyen, S. T.; Ruoff, R. S. Graphene-Based Composite Materials. *Nature* **2006**, *442*, 282−286.
(2) Gao, Y.; Wang, Q.; Wang, J.; Huang, L.; Yan, X.; Zhang, X.; He, Q.; Xing, Z.; Guo, Z. Synthesis of Highly Efficient Flame Retardant HDPE Nanocomposites with Inorgano-LDH as Nanofiller Using

DOI: 10.1021/am5082183
ACS Appl. Mater. Interfaces 2015, 7, 6125−6138

Solvent Mixing Method. *ACS Appl. Mater. Interfaces* **2014**, *6* (7), 5094−5104.
(3) Wang, Q.; Zhang, X.; Wang, C. J.; Zhu, J.; Guo, Z.; O'Hare, D. Polypropylene/Layered Double Hydroxide Nanocomposites. *J. Mater. Chem.* **2012**, *22*, 19113−19121.
(4) He, Q.; Yuan, T.; Luo, Z.; Haldolaarachchige, N.; Young, D. P.; Wei, S.; Guo, Z. Morphology and Phase Controlled Cobalt Nanostructures in Magnetic Polypropylene Nanocomposites: The Role of Alkyl Chain-Length in Maleic Anhydride Grafted Polypropylene. *Chem. Commun.* **2013**, *49*, 2679−2681.
(5) Gu, H.; Tadakamalla, S.; Huang, Y.; Colorado, H. A.; Luo, Z.; Haldolaarachchige, N.; Young, D. P.; Wei, S.; Guo, Z. Polyaniline Stabilized Magnetite Nanoparticle Reinforced Epoxy Nanocomposites. *ACS Appl. Mater. Interfaces* **2012**, *4*, 5613−5624.
(6) Chen, M.; Qu, H.; Zhu, J.; Luo, Z.; Khasanov, A.; Kucknoor, A. S.; Haldolaarachchige, N.; Young, D. P.; Wei, S.; Guo, Z. Magnetic Electrospun Fluorescent Polyvinylpyrrolidone Nanocomposite Fibers. *Polymer* **2012**, *53*, 4501−4511.
(7) Guo, Z.; Wei, S.; Shedd, B.; Scaffaro, R.; Pereira, T.; Hahn, H. T. Particle Surface Engineering Effect on The Mechanical, Optical and Photoluminescent Properties of ZnO/Vinyl-Ester Resin Nanocomposites. *J. Mater. Chem.* **2007**, *17*, 806−813.
(8) Wei, H.; Yan, X.; Wu, S.; Luo, Z.; Wei, S.; Guo, Z. Electropolymerized Polyaniline Stabilized Tungsten Oxide Nanocomposite Films: Electrochromic Behavior and Electrochemical Energy Storage. *J. Phys. Chem. C* **2012**, *116*, 25052−25064.
(9) Wei, H.; Yan, X.; Li, Y.; Gu, H.; Wu, S.; Ding, K.; Wei, S.; Guo, Z. Electrochromic Poly(DNTD)/WO_3 Nanocomposite Films via Electropolymerization. *J. Phys. Chem. C* **2012**, *116*, 16286−16293.
(10) Zhu, J.; Wei, S.; Alexander, M. J.; Dang, T. D.; Ho, T. C.; Guo, Z. Electrochromic Properties of Poly(p-phenylenebenzobisthiazole) Thin Films Embedded with Nano-WO_3. *Adv. Funct. Mater.* **2010**, *20*, 3076−3084.
(11) Zhang, X.; He, Q.; Gu, H.; Guo, Z.; Wei, S. Polyaniline Stabilized Barium Titanate Nanoparticles Reinforced Epoxy Nanocomposites with High Dielectric Permittivity and Reduced Flammability. *J. Mater. Chem. C* **2013**, *1*, 2886−2899.
(12) Gu, H.; Huang, Y.; Zhang, X.; Wang, Q.; Zhu, J.; Shao, L.; Haldolaarachchige, N.; Young, D. P.; Wei, S.; Guo, Z. Magnetoresistive Polyaniline-Magnetite Nanocomposites with Negative Dielectrical Properties. *Polymer* **2012**, *53*, 801−809.
(13) Coleman, J. N.; Khan, U.; Blau, W. J.; Gun'ko, Y. K. *Carbon* **2006**, *44*, 1624−1652.
(14) Ávila-Orta, C. A.; R.-L, C. E.; Dávila-Rodríguez, M. V.; Aguirre-Figueroa, Y. A.; Cruz-Delgado, V. J.; Neira-Velázquez, M. G.; Medellín-Rodríguez, F. J.; Hsiao, B. S. *Int. J. Polym. Mater.* **2013**, *62*, 635−641.
(15) Kashiwagi, T.; Grulke, E.; Hilding, J.; Groth, K.; Harris, R.; Butler, K.; Shields, J.; Kharchenko, S.; Douglas, J. *Polymer* **2004**, *45*, 4227−4239.
(16) Li, J.; Ma, P. C.; Chow, W. S.; To, C. K.; Tang, B. Z.; Kim, J. K. Correlations between Percolation Threshold, Dispersion State, and Aspect Ratio of Carbon Nanotubes. *Adv. Funct. Mater.* **2007**, *17*, 3207−3215.
(17) Xin, F.; Li, L. *J. Compos. Mater.* **2012**, *15*, 1−9.
(18) Seo, M.-K.; Park, S.-J. Electrical Resistivity and Rheological Behaviors of Carbon Nanotubes-Filled Polypropylene Composites. *Chem. Phys. Lett.* **2004**, *395*, 44−48.
(19) Koval'chuk, A. A.; Shchegolikhin, A. N.; Shevchenko, V. G.; Nedorezova, P. M.; Klyamkina, A. N.; Aladyshev, A. M. Synthesis and Properties of Polypropylene/Multiwall Carbon Nanotube Composites. *Macromolecules* **2008**, *41*, 3149−3156.
(20) UreÃa-Benavides, E. E.; Kayatin, M. J.; Davis, V. A. Dispersion and Rheology of Multiwalled Carbon Nanotubes in Unsaturated Polyester Resin. *Macromolecules* **2013**, *46*, 1642−1650.
(21) Zhu, J.; Wei, S.; Yadav, A.; Guo, Z. Rheological Behaviors and Electrical Conductivity of Epoxy Resin Nanocomposites Suspended with In-Situ Stabilized Carbon Nanofibers. *Polymer* **2010**, *51*, 2643−2651.
(22) Lee, S. H.; Cho, E.; Jeon, S. H.; Youn, J. R. Rheological and Electrical Properties of Polypropylene Composites Containing Functionalized Multi-Walled Carbon Nanotubes and Compatibilizers. *Carbon* **2007**, *45*, 2810−2822.
(23) Bose, S.; Khare, R. A.; Moldenaers, P. Assessing The Strengths and Weaknesses of Various Types of Pre-treatments of Carbon Nanotubes on The Properties of Polymer/Carbon Nanotubes Composites: A Critical Review. *Polymer* **2010**, *51*, 975−993.
(24) Kim, Y. J.; Shin, T. S.; Choi, H. D.; Kwon, J. H.; Chung, Y.-C.; Yoon, H. G. Electrical Conductivity of Chemically Modified Multiwalled Carbon Nanotube/Epoxy Composites. *Carbon* **2005**, *43*, 23−30.
(25) Zhang, S.; Fan, W.; Panoiu, N. C.; Malloy, K. J.; Osgood, R. M.; Brueck, S. R. J. Experimental Demonstration of Near-Infrared Negative-Index Metamaterials. *Phys. Rev. Lett.* **2005**, *95*, 137404.
(26) Pendry, J. B.; MartÃn-Moreno, L.; Garcia-Vidal, F. J. Mimicking Surface Plasmons with Structured Surfaces. *Science* **2004**, *305*, 847−848.
(27) Hilt, O.; Brom, H. B.; Ahlskog, M. Localized and Delocalized Charge Transport in Single-Wall Carbon-Nanotube Mats. *Phys. Rev. B* **2000**, *61*, R5129−R5132.
(28) Zhu, J.; Wei, S.; Zhang, L.; Mao, Y.; Ryu, J.; Karki, A. B.; Young, D. P.; Guo, Z. Polyaniline-Tungsten Oxide Metacomposites with Tunable Electronic Properties. *J. Mater. Chem.* **2011**, *21*, 342−348.
(29) Zhu, J.; Wei, S.; Ryu, J.; Guo, Z. Strain-Sensing Elastomer/Carbon Nanofiber "Metacomposites. *J. Phys. Chem. C* **2011**, *115*, 13215−13222.
(30) Hoffman, A. J.; Alekseyev, L.; Howard, S. S.; Franz, K. J.; Wasserman, D.; Podolskiy, V. A.; Narimanov, E. E.; Sivco, D. L.; Gmachl, C. Negative Refraction in Semiconductor Metamaterials. *Nat. Mater.* **2007**, *6*, 946−950.
(31) Pendry, J. B.; Holden, A. J.; Stewart, W. J.; Youngs, I. Extremely Low Frequency Plasmons in Metallic Mesostructures. *Phys. Rev. Lett.* **1996**, *76*, 4773−4776.
(32) Dolgov, O. V.; Kirzhnits, D. A.; Maksimov, E. G. On an Admissible Sign of The Static Dielectric Function of Matter. *Rev. Mod. Phys.* **1981**, *53*, 81−93.
(33) Baughman, R. H.; Zakhidov, A. A.; de Heer, W. A. Carbon Nanotubes–the Route Toward Applications. *Science* **2002**, *297*, 787−792.
(34) Popov, V. N. Carbon Nanotubes: Properties and Application. *Mater. Sci. Eng., R* **2004**, *43*, 61−102.
(35) Wang, M.; Wang, W.; Liu, T.; Zhang, W.-D. Melt Rheological Properties of Nylon 6/Multi-Walled Carbon Nanotube Composites. *Compos. Sci. Technol.* **2008**, *68*, 2498−2502.
(36) Sun, L.; Boo, W.-J.; Liu, J.; Clearfield, A.; Sue, H.-J.; Verghese, N. E.; Pham, H. Q.; Bicerano, J. Effect of Nanoplatelets on the Rheological Behavior of Epoxy Monomers. *Macromol. Mater. Eng.* **2009**, *294*, 103−113.
(37) Sun, L.; Liu, J.; Kirumakki, S. R.; Schwerdtfeger, E. D.; Howell, R. J.; Al-Bahily, K.; Miller, S. A.; Clearfield, A.; Sue, H.-J. Polypropylene Nanocomposites Based on Designed Synthetic Nanoplatelets. Chemistry of Materials. *Chem. Mater.* **2009**, *21*, 1154−1161.
(38) Huang, S.; Wang, M.; Liu, T.; Zhang, W.-D.; Tjiu, W. C.; He, C.; Lu, X. Morphology, Thermal, and Rheological Behavior of Nylon 11/Multi-Walled Carbon Nanotube Nanocomposites Prepared by Melt Compounding. *Polym. Eng. Sci.* **2009**, *49*, 1063−1068.
(39) Lee, W. D.; Im, S. S.; Lim, H.-M.; Kim, K.-J. Preparation and Properties of Layered Double Hydroxide/Poly(ethylene terephthalate) Nanocomposites by Direct Melt Compounding. *Polymer* **2006**, *47*, 1364−1371.
(40) Zhang, X.; Alloul, O.; Zhu, J.; Luo, Z.; Colorado, H. A.; Haldolaarachchige, N.; Young, D. P.; Shen, T. D.; He, Q.; Wei, S.; Guo, Z. Iron Core Carbon Shell Nanoparticles Reinforced Electrically Conductive Magnetic Epoxy Resin Nanocomposites with Reduced Flammability. *RSC Adv.* **2013**, *3*, 9453−9464.
(41) Zhang, X.; He, Q.; Gu, H.; Colorado, H. A.; Wei, S.; Guo, Z. Flame Retardant Conductive Epoxy Resin Nanocomposites Re-

DOI: 10.1021/am5082183
ACS Appl. Mater. Interfaces 2015, 7, 6125−6138

inforced with Various Polyaniline Nanostructures. *ACS Appl. Mater. Interfaces* **2013**, *5*, 898−910.
(42) Tuteja, A.; Duxbury, P. M.; Mackay, M. E. Multifunctional Nanocomposites with Reduced Viscosity. *Macromolecules* **2007**, *40*, 9427−9434.
(43) Jain, S.; Goossens, J. G. P.; Peters, G. W. M.; van Duin, M.; Lemstra, P. J. Strong Decrease in Viscosity of Nanoparticle-Filled Polymer Melts through Selective Adsorption. *Soft Matter* **2008**, *4*, 1848−1854.
(44) Thanpitcha, T.; Li, Z.; Rujiravanit, R.; Sirivat, A.; Jamieson, A. Anomalous Rheology of Polypyrrole Nanoparticle/Alginate Suspensions: Effect of Solids Volume Fraction, Particle Size, and Electronic State. *Rheol. Acta* **2011**, *50*, 809−823.
(45) Yan, D.; Wang, W. J.; Zhu, S. Effect of Long Chain Branching on Rheological Properties of Metallocene Polyethylene. *Polymer* **1999**, *40*, 1737−1744.
(46) Jaber, E.; Luo, H.; Li, W.; Gersappe, D. Network Formation in Polymer Nanocomposites under Shear. *Soft Matter* **2011**, *7*, 3852−3860.
(47) Green, P. F.; Mills, P. J.; PalmstrÃm, C. J.; Mayer, J. W.; Kramer, E. J. Limits of Reptation in Polymer Melts. *Phys. Rev. Lett.* **1984**, *53*, 2145−2148.
(48) Bubeck, R. A. Structure-Property Relationships in Metallocene Polyethylenes. *Mater. Sci. Eng., R* **2002**, *39*, 1−28.
(49) Sternstein, S. S.; Zhu, A.-J. Reinforcement Mechanism of Nanofilled Polymer Melts As Elucidated by Nonlinear Viscoelastic Behavior. *Macromolecules* **2002**, *35*, 7262−7273.
(50) Sinha Ray, S.; Maiti, P.; Okamoto, M.; Yamada, K.; Ueda, K. New Polylactide/Layered Silicate Nanocomposites. 1. Preparation, Characterization, and Properties. *Macromolecules* **2002**, *35*, 3104−3110.
(51) Hyun, Y. H.; Lim, S. T.; Choi, H. J.; Jhon, M. S. Rheology of Poly(ethylene oxide)/Organoclay Nanocomposites. *Macromolecules* **2001**, *34*, 8084−8093.
(52) Fu, B. X.; Gelfer, M. Y.; Hsiao, B. S.; Phillips, S.; Viers, B.; Blanski, R.; Ruth, P. Physical Gelation in Ethylene-Propylene Copolymer Melts Induced by Polyhedral Oligomeric Silsesquioxane (POSS) Molecules. *Polymer* **2003**, *44*, 1499−1506.
(53) Zhu, J.; Wei, S.; Li, Y.; Sun, L.; Haldolaarachchige, N.; Young, D. P.; Southworth, C.; Khasanov, A.; Luo, Z.; Guo, Z. Surfactant-Free Synthesized Magnetic Polypropylene Nanocomposites: Rheological, Electrical, Magnetic, and Thermal Properties. *Macromolecules* **2011**, *44*, 4382−4391.
(54) Chen, X.; Wei, S.; Yadav, A.; Patil, R.; Zhu, J.; Ximenes, R.; Sun, L.; Guo, Z. Poly(propylene)/Carbon Nanofiber Nanocomposites: Ex Situ Solvent-Assisted Preparation and Analysis of Electrical and Electronic Properties. *Macromol. Mater. Eng.* **2011**, *296*, 434−443.
(55) Thomann, R.; Wang, C.; Kressler, J. r.; MÃlhaupt, R. On the γ-Phase of Isotactic Polypropylene. *Macromolecules* **1996**, *29*, 8425−8434.
(56) Mezghani, K.; Phillips, P. J. The γ-Phase of High Molecular Weight Isotactic Polypropylene: III. The Equilibrium Melting Point and the Phase Diagram. *Polymer* **1998**, *39*, 3735−3744.
(57) Song, P. A.; Liu, L.; Huang, G.; Fu, S.; Yu, Y.; Guo, Q. Facile Fabrication of Polyolefin/Carbon Nanotube Composites via in Situ Friedel−Crafts Polyalkylation: Structure and Properties. *Ind. Eng. Chem. Res.* **2013**, *52*, 14384−14395.
(58) Hoffman, J. D.; Miller, R. L.; Marand, H.; Roitman, D. B. Relationship between The Lateral Surface Free Energy Sigma and The Chain Structure of Melt-Crystallized Polymers. *Macromolecules* **1992**, *25*, 2221−2229.
(59) Papageorgiou, G. Z.; Achilias, D. S.; Bikiaris, D. N.; Karayannidis, G. P. Crystallization Kinetics and Nucleation Activity of Filler in Polypropylene/Surface-Treated SiO_2 Nanocomposites. *Thermochim. Acta* **2005**, *427*, 117−128.
(60) Tsuji, H.; Takai, H.; Saha, S. K. Isothermal and Non-Isothermal Crystallization Behavior of Poly(l-lactic acid): Effects of Stereocomplex as Nucleating Agent. *Polymer* **2006**, *47*, 3826−3837.
(61) Vyazovkin, S.; Stone, J.; Sbirrazzuoli, N. Hoffman-Lauritzen Parameters for Non-Isothermal Crystallization of Poly(ethylene terephthalate) and Poly(ethylene oxide) Melts. *J. Therm. Anal. Calorim.* **2005**, *80*, 177−180.
(62) Welch, P.; Muthukumar, M. Molecular Mechanisms of Polymer Crystallization from Solution. *Phys. Rev. Lett.* **2001**, *87*, 218302.
(63) Grady, B. P.; Pompeo, F.; Shambaugh, R. L.; Resasco, D. E. Nucleation of Polypropylene Crystallization by Single-Walled Carbon Nanotubes. *J. Phys. Chem. B* **2002**, *106*, 5852−5858.
(64) Li, H.; Huneault, M. A. Effect of Nucleation and Plasticization on the Crystallization of Poly(lactic acid). *Polymer* **2007**, *48*, 6855−6866.
(65) Foresta, T.; Piccarolo, S.; Goldbeck-Wood, G. Competition between α and γ Phases in Isotactic Polypropylene: Effects of Ethylene Content and Nucleating Agents at Different Cooling Rates. *Polymer* **2001**, *42*, 1167−1176.
(66) He, Q.; Yuan, T.; Zhang, X.; Luo, Z.; Haldolaarachchige, N.; Sun, L.; Young, D. P.; Wei, S.; Guo, Z. Magnetically Soft and Hard Polypropylene/Cobalt Nanocomposites: Role of Maleic Anhydride Grafted Polypropylene. *Macromolecules* **2013**, *46*, 2357−2368.
(67) Seo, M.-K.; Lee, J.-R.; Park, S.-J. Crystallization Kinetics and Interfacial Behaviors of Polypropylene Composites Reinforced with Multi-walled Carbon Nanotubes. *Mater. Sci. Eng., A* **2005**, *404*, 79−84.
(68) Li, Y.; Zhu, J.; Wei, S.; Ryu, J.; Wang, Q.; Sun, L.; Guo, Z. Poly(propylene) Nanocomposites Containing Different Carbon Nanostructures. *Macromol. Chem. Phys.* **2011**, *212*, 2429−2438.
(69) Ounaies, Z.; Park, C.; Wise, K. E.; Siochi, E. J.; Harrison, J. S. Electrical Properties of Single Wall Carbon Nanotube Reinforced Polyimide Composites. *Compos. Sci. Technol.* **2003**, *63*, 1637−1646.
(70) Kilbride, B. E.; Coleman, J. N.; Fraysse, J.; Fournet, P.; Cadek, M.; Drury, A.; Hutzler, S.; Roth, S.; Blau, W. J. Experimental Observation of Scaling Laws for Alternating Current and Direct Current Conductivity in Polymer-Carbon Nanotube Composite Thin Films. *Jpn. J. Appl. Phys.* **2002**, *92*, 4024−4030.
(71) Alshehri, A. H.; Jakubowska, M.; Sloma, M.; Horaczek, M.; Rudka, D.; Free, C.; David Carey, J. Electrical performance of carbon nanotube-polymer composites at frequencies up to 220 GHz. *Appl. Phys. Lett.* **2011**, *99*, 153109.
(72) Guo, Z.; Shin, K.; Karki, A.; Young, D.; Kaner, R.; Hahn, H. Fabrication and Characterization of Iron Oxide Nanoparticles Filled Polypyrrole Nanocomposites. *J. Nanopart. Res.* **2009**, *11*, 1441−1452.
(73) Zhang, X.; Wei, S.; Haldolaarachchige, N.; Colorado, H. A.; Luo, Z.; Young, D. P.; Guo, Z. Magnetoresistive Conductive Polyaniline - Barium Titanate Nanocomposites with Negative Permittivity. *J. Phys. Chem. C* **2012**, *116*, 15731−15740.
(74) Seidel, G. D.; Lagoudas, D. C. A Micromechanics Model for the Electrical Conductivity of Nanotube-Polymer Nanocomposites. *J. Compos. Mater.* **2009**, *43*, 917−941.
(75) Hu, L.; Hecht, D. S.; Grüner, G. Percolation in Transparent and Conducting Carbon Nanotube Networks. *Nano Lett.* **2004**, *4*, 2513−2517.
(76) Tauc, J. Absorption Edge and Internal Electric Fields in Amorphous Semiconductors. *Mater. Res. Bull.* **1970**, *5*, 721−729.
(77) Hjelm, A.; Granqvist, C. G.; Wills, J. M. Electronic Structure and Optical Properties of WO_3, $LiWO_3$, $NaWO_3$, and HWO_3. *Phys. Rev. B* **1996**, *54*, 2436−2445.
(78) Serpone, N.; Lawless, D.; Khairutdinov, R. Size Effects on the Photophysical Properties of Colloidal Anatase TiO_2 Particles: Size Quantization versus Direct Transitions in This Indirect Semiconductor? *J. Phys. Chem.* **1995**, *99*, 16646−16654.
(79) Tzolov, M. B.; Kuo, T.-F.; Straus, D. A.; Yin, A. Xu. Carbon Nanotubes-Silicon Heterojunction Arrays and Infrared Photocurrent Responses. *J. Phys. Chem. C* **2007**, *111*, 5800−5804.
(80) Dukovic, G.; Wang, F.; Song, D.; Sfeir, M. Y.; Heinz, T. F.; Brus, L. E. Structural Dependence of Excitonic Optical Transitions and Band-Gap Energies in Carbon Nanotubes. *Nano Lett.* **2005**, *5*, 2314−2318.

DOI: 10.1021/am5082183
ACS Appl. Mater. Interfaces 2015, 7, 6125−6138

(81) Minot, E. D.; Yaish, Y.; Sazonova, V.; Park, J.-Y.; Brink, M.; McEuen, P. L. Tuning Carbon Nanotube Band Gaps with Strain. *Phys. Rev. Lett.* **2003**, *90*, 156401.
(82) Martel, R.; Schmidt, T.; Shea, H. R.; Hertel, T.; Avouris, P. Single- and Multi-Wall Carbon Nanotube Field-Effect Transistors. *Appl. Phys. Lett.* **1998**, *73*, 2447−2449.
(83) Gülseren, O.; Yildirim, T.; Ciraci, S.; Kılıç, Ç. Reversible Band-Gap Engineering in Carbon Nanotubes by Radial Deformation. *Phys. Rev. B* **2002**, *65*, 155410.
(84) Yang, L.; Anantram, M. P.; Han, J.; Lu, J. P. Band-gap Change of Carbon Nanotubes: Effect of Small Uniaxial and Torsional Strain. *Phys. Rev. B* **1999**, *60*, 13874−13878.
(85) Ni, Z. H.; Yu, T.; Lu, Y. H.; Wang, Y. Y.; Feng, Y. P.; Shen, Z. X. Uniaxial Strain on Graphene: Raman Spectroscopy Study and Band-Gap Opening. *ACS Nano* **2008**, *2*, 2301−2305.
(86) Leeuw, T. K.; Tsyboulski, D. A.; Nikolaev, P. N.; Bachilo, S. M.; Arepalli, S.; Weisman, R. B. Strain Measurements on Individual Single-Walled Carbon Nanotubes in a Polymer Host: Structure-Dependent Spectral Shifts and Load Transfer. *Nano Lett.* **2008**, *8*, 826−831.
(87) Rashidi-Huyeh, M.; Palpant, B. Counterintuitive Thermo-Optical Response of Metal-dielectric Nanocomposite Materials as a Result of Local Electromagnetic Field Enhancement. *Phys. Rev. B* **2006**, *74*, 075405.
(88) Nagel, S. R.; Schnatterly, S. E. Frequency Dependence of the Drude Relaxation Time in Metal Films. *Phys. Rev. B* **1974**, *9*, 1299−1303.
(89) Johnson, P. B.; Christy, R. W. Optical Constants of the Noble Metals. *Phys. Rev. B* **1972**, *6*, 4370−4379.
(90) Enoch, S.; Tayeb, G. r.; Sabouroux, P.; Guérin, N.; Vincent, P. A Metamaterial for Directive Emission. *Phys. Rev. Lett.* **2002**, *89*, 213902.
(91) Kohlman, R. S.; Joo, J.; Wang, Y. Z.; Pouget, J. P.; Kaneko, H.; Ishiguro, T.; Epstein, A. J. Drude Metallic Response of Polypyrrole. *Phys. Rev. Lett.* **1995**, *74*, 773−776.
(92) Novotny, L.; Hecht, B. *Surface plasmons Principles of Nano-Optics*; Cambridge University Press: New York, 2006.
(93) Hwang, E. H.; Das Sarma, S. Dielectric Function, Screening, and Plasmons in Two-Dimensional Graphene. *Phys. Rev. B* **2007**, *75*, 205418.
(94) Li, B.; Sui, G.; Zhong, W.-H. Single Negative Metamaterials in Unstructured Polymer Nanocomposites Toward Selectable and Controllable Negative Permittivity. *Adv. Mater.* **2009**, *21*, 4176−4180.
(95) Zhu, J.; Luo, Z.; Wu, S.; Haldolaarachchige, N.; Young, D. P.; Wei, S.; Guo, Z. Magnetic Graphene Nanocomposites: Electron Conduction, Giant Magnetoresistance and Tunable Negative Permittivity. *J. Mater. Chem.* **2012**, *22*, 835−844.

DOI: 10.1021/am5082183
ACS Appl. Mater. Interfaces 2015, 7, 6125−6138